5
Colloidal MoS_2 Quantum Dots for High-performance Low Power Resistive Memory Devices with Excellent Temperature Stability

Conventional memory technologies are facing enormous problems with downscaling hence unable to fulfil the requirement of big data storage generated by a huge explosion of digital information. The silicon-based technologies are facing several theoretical and practical limitations upon downscaling. Also, the Von Neumann architecture used in the current computes has a separate processing unit and storage unit. As the processing unit and storage units are separated and connected by buses, the data transfer speed is limited and this architecture consumes a lot of power. Therefore, it is essentially needed to design universal memory with high-density data storage, fast operation speed, the capacity of in-memory computing and low power consumption. RRAM is one of the most emerging technologies for next-generation computing data storage owing to high-density stacking, ultrafast switching speed, high non-volatility, multilevel data storage, low power consumption and simple device structure. In the previous chapters, the CdSe QDs-PVP composites-based RRAM devices exhibited excellent resistive switching behavior with low power consumption. But CdSe is a toxic material and has been found to be a human carcinogen. Therefore, the use of less toxic and non-carcinogens materials in RRAM devices is highly preferable. MoS_2 has been found to be less toxic and non-carcinogen. In this work, colloidal MoS_2 quantum dots (QDs) embedded in an insulating matrix of poly-(4vinylpyridine) (PVP) were used as an active layer to fabricate an RRAM device. The MoS_2 QDs-PVP-based RRAM device reveals excellent nonvolatile RS behavior with a maximum I_{ON}/I_{OFF} of 10^5. High endurance, long retention time and successive "write-read-erase-read" cycles indicate high-performance RRAM characteristics. The ultimate power consumption by this RRAM device is considerably low for energy saving. In addition, the MoS_2 QDs-PVP-based device shows RS behavior even at 130 °C. High I_{ON}/I_{OFF}, low operating power, high endurance, long retention time and excellent stability with temperatures reveal that MoS_2 QDs-PVP-based device can be a promising candidate for a high-performance, low-power RRAM device that can be operated at a relatively higher temperature.

5.1 Introduction

The modern big data era and the huge explosion of digital information led to the requirement for high-density nonvolatile data storage devices with fast operation speed and low power consumption [Gao et al., 2019; Lv et al., 2020; Wang et al., 2020a]. The silicon-based technologies are facing several theoretical and practical limitations upon downscaling [Cho et al., 2011a; Lin et al., 2014; Wang et al., 2020a]. Also, the Von Neumann architecture used in the current computers has a separate processing unit and storage unit [Schulz, 1999; Wong et al., 2015]. As the processing unit and storage units are separated and connected by buses, the data transfer speed is limited and this architecture consumes a lot of power. Therefore, it is essentially needed to design universal memory with high-density data storage, fast operation speed, the capacity of in-memory computing and low power consumption. RRAM is one of the most emerging technologies for future computing data storage [Khan et al., 2021; Sebastian et al., 2020]. High-density stacking, ultrafast switching speed, high non-volatility, multilevel data storage, low power consumption, the capability of in-memory computing and simple device structure make

RRAM devices leave the hard disk drive (HDD), SRAM, and DRAM behind [Chen et al., 2020a; Kwon et al., 2010; Scott et al., 2007; Yang et al., 2009c; Zhang et al., 2016b].

Oxide-based materials [Kwon et al., 2010; Wedig et al., 2016], organic molecules [Gao et al., 2019; Vyas et al., 2016] and polymers [Chang et al., 2022; Liu et al., 2019a], metal chalcogenides quantum dots [Chen et al., 2020a; Das et al., 2022] are the potential candidates for the active materials of RRAM devices over the past few decades. However, after the discovery of graphene, graphene oxides (GO) and layered transition metal di-chalcogenides (TMDCs), nanoparticles came into the picture as active materials in RRAM devices [Bhattacharjee et al., 2020; Pal et al., 2020; Wu et al., 2019; Yan et al., 2018]. Molybdenum disulfide (MoS_2) is one of the most studied materials owing to its marvellous optical and electronic properties [Kang et al., 2020]. Single-layer and few-layer MoS_2 have been extensively used in field-effect transistors [Conti et al., 2020], photodetectors [Selamneni et al., 2021], gas sensing devices [Goel et al., 2021; Niu et al., 2021], energy storage devices [Li et al., 2020] and photocatalytic applications [Thomas et al., 2021]. Oxide-based memristors are limited by poor control over filament formation and external applied biasing voltage [Han et al., 2017]. Organic memristors are easy to fabricate and low cost but less stable in ambient [Lee et al., 2017]. Recently popular halide perovskite-based materials have been found to be good as an active layer in memristors, but poor stability in the ambient limits their application in practical RRAMs [Kang et al., 2021; Paramanik et al., 2022]. CdX (X=S, Se) QDs and CdX QDs core-shell with other metal chalcogenides QDs show good RS behavior but these elements are very toxic and human carcinogens [Guo et al., 2020; Pradhan et al., 2021]. Therefore, GO and MoS_2, which are less toxic and non-carcinogens, became popular as an active layer of memristors. Nanocomposites of MoS_2 nanosheet-GO and MoS_2- polyvinylpyrrolidone exhibited RS behavior [Liu et al., 2012a; Wu et al., 2019; Yin et al., 2013; Zhang et al., 2016a], but I_{ON}/I_{OFF} was limited to 100. Hydrothermally grown MoS_2 QDs with poly(methylsilsesquioxane) exhibited RS with high I_{ON}/I_{OFF}, but operating power was large [Veeramalai et al., 2019]. Several studies reveal that composites of MoS_2 nanosheet, nanoparticles (NPs) and QDs with organic polymers show good nonvolatile RS behavior [Bhattacharjee et al., 2017; Fan et al., 2017a, 2018]. Another two-dimensional layered material (2DLM) hexagonal boron-nitride and polymethyl methacrylate (PMMA) based nanocomposite showed excellent WORM type memory behavior [Li et al., 2021]. Also, the heterostructure of 2DLM with a memory unit and a selector can be used for RRAM technology [Chiang et al., 2021]. Artificial synapse type RS behavior has been explored recently using MoS_2 QDs and nanoflakes [Manamel et al., 2021; Thomas et al., 2020].

Most of the MoS_2 NPs and QDs were achieved using the hydrothermal or solvothermal method or ultra-sonication assisted liquid exfoliation followed by centrifugation techniques. In these methods, it is difficult to control the uniform size distribution of MoS_2 QDs. In this work, colloidal MoS_2 QDs were synthesized by the reduction of ammonium tetrathiomolybdate [Lin et al., 2015a] and PVP was blended with MoS_2 QDs to fabricate the MoS_2 QDs-PVP RRAM device. The fabricated device shows excellent nonvolatile RS behavior with high I_{ON}/I_{OFF}, high endurance, long retention time and low operating power. In most of the previous MoS_2-based RRAM devices, RS characteristics were measured at room temperature. A device needs to be stable when operated in a hot region such as Rajasthan in India, where the ambient temperature goes ~50 °C in summer. The effect of temperature on the RS behavior in MoS_2 QDs-based RRAM devices is yet to be explored.

In this chapter, the stability of the RS characteristics of the MoS_2 QDs-PVP device at different temperatures by simultaneously heating the device during the I-V measurement has been explored. Our MoS_2 QDs-PVP-based RRAM device shows RS behavior up to 130 °C. This study reveals that the fabricated MoS_2 QDs-PVP RRAM device is a potential candidate for high-performance, low-power resistive memory devices which can be operated in extremely hot weather conditions.

5.2 Experimental Section

In this section, the detailed synthesis procedure of materials with the used chemical list and the device fabrication process have been discussed.

5.2.1 List of Chemicals Used

Ammonium tetrathiomolybdate ($(NH_4)_2MoS_4$) (99.97% trace metal basis, Sigma Aldrich), 1-octadecene (ODE) (technical grade, 90%, Sigma Aldrich), oleic acid (OA) (≥ 99%, Sigma Aldrich), oleyl amine (OAM) (technical grade 70%, Sigma Aldrich), Poly(4-vinyl pyridine) (PVP, M.W. ~ 60,000, Sigma Aldrich), acetone, methanol and chloroform were used.

5.2.2 Synthesis of MoS_2 QDs

Colloidal MoS_2 QDs were synthesized by the reduction of ammonium tetrathiomolybdate ($(NH_4)_2MoS_4$) at 250 °C under a nitrogen atmosphere [Lin et al., 2015a]. In this process, 0.1 mM of $(NH_4)_2MoS_4$, 2 mL oleic acid (OA), 6 mL oleylamine (OAM) and 12 mL ODE were loaded into a 100 mL three-necked flask. The reaction flask was then evacuated using a vacuum pump and no leakages were confirmed. The mixture was heated with continuous stirring in a magnetic stirrer hotplate at 120 °C under vacuum using a standard schlenk line for 2 hours and 30 minutes to remove moisture and to obtain a homogeneous solution. The reaction mixture was then purged by dry N_2 gas and heated to 250 °C with a heating rate of 5 °C / 10 min. At 250 °C, the reaction mixture was kept for 3 hours for the growth of particles and then cooled naturally to RT. When the reaction bath was cooled to RT, the black color crude solutions were taken into test tubes. Acetone was added dropwise into the crude solution in test tubes to precipitate the QD particles and then centrifuge at 6000 rpm for 5 min. To collect the QDs, upper transparent supernatant was removed and precipitated particles were rinsed with methanol and dispersed in chloroform. This cleaning process was repeated 2 more times to remove excess OA, OAM and other unreacted products. Finally, the precipitated MoS_2 QDs were dried under nitrogen and redispersed in chloroform for further use. Here, OAM is used as a reducing agent for $(NH_4)_2MoS_4$ and as well as a stabilizing agent along with OA to control the size of the QDs. The Figure 5.1 shows the schematic of the synthesis procedure step by step.

5.2.3 Fabrication of RRAM Device

For device fabrication, ITO-coated glass substrates were etched using zinc dust and hydrochloric acid to form an ITO strip in the middle of the substrates. Etched substrates were then cleaned by ultrasonication in a soap solution, DI water, acetone, DI water and methanol for 15 min each and subsequently, this process was repeated three times. The cleaned substrates were then dried using an N_2 gun. PVP and as-prepared MoS_2 QDs were mixed in a weight ratio of 2:1 in chloroform and were ultrasonicated for 30 min prior to the spin coating process. The MoS_2 QDs-PVP mixture was then spin-coated on the cleaned ITO substrates at 1000 rpm for 40 s and then dried at 80 °C in a hotplate for 30 min. Al top electrodes with a crossbar pattern were deposited using a metal shadow mask in a thermal deposition system at a base pressure of 4×10^{-6} mbar with continuous rotating of the substrates for uniform metal deposition. The structure of device is shown in Figure 5.2 schematically.

5.2.4 Characterizations techniques

XRD pattern was studied in Bruker AXS model (D8 Advance) X-Ray diffractometer. XPS spectra were taken in a Thermo Scientific K-Alpha+ spectrometer within ultrahigh-vacuum conditions (10^{-9} mbar). Al Kα (1486.6 eV) was utilized as the monochromatic X-ray source with a pass energy of 50 eV for the individual core levels. Absorption spectra were obtained in a Varian Carry 4000 UV-Vis spectrophotometer. AFM images were obtained using Park Systems XE-70 with non-contact mode. HRTEM images were collected in JEOL JEM 2200FES. The image of the cross-section of the device was taken in FESEM NNS 450 instrument. The I-V measurements of the device were carried out in a homemade two-terminal probe station with a substrate heater using Keithley 6430 SUB-FEMTOAMP sourcemeter. The active area of each cell was 1.2 × 1.2 mm^2.

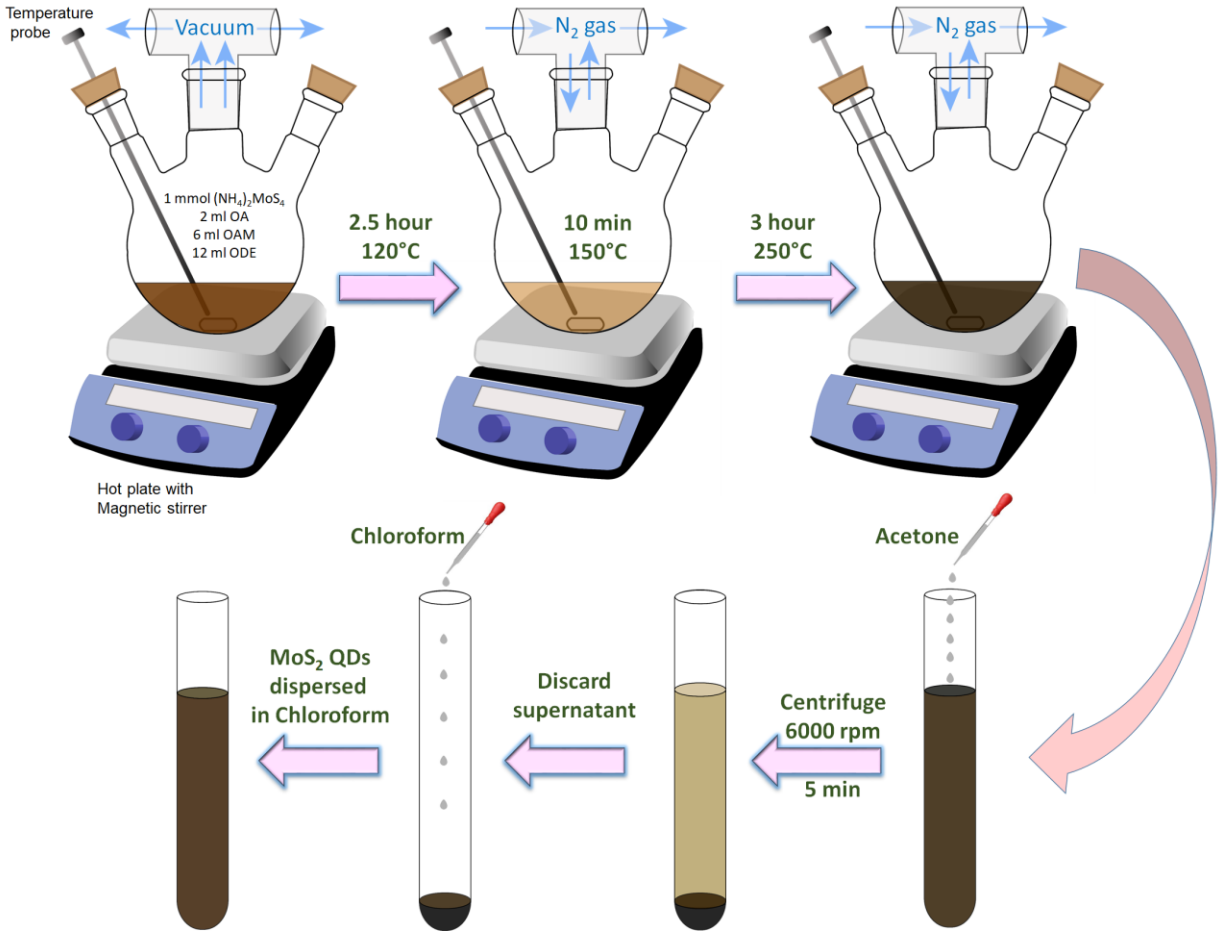


Figure 5.1: Schematic illustration of the synthesis procedure of MoS_2 QDs.

5.3 Results and Discussions

In this section, the results from materials characterizations and device characterizations have been discussed and analyzed.

5.3.1 Characterizations of Material

Figure 5.3a shows the XRD pattern of the as-synthesized MoS_2 QDs, which were dropped cast on a glass slide. The diffraction peak at 14.46°, which is the main characteristic peak of pure MoS_2 hexagonal phase (JCPDS card no. 37-1492) corresponding to the (002) plane and at 28.56° corresponding to the (004) plane [Bhattacharjee et al., 2017] have been observed in XRD. Other peaks are too weak to distinguish because the few layers of QDs are too thin to be detected in XRD.

Figure 5.3b shows the absorption spectra of MoS_2 QDs where a sharp peak at 406 nm has been observed, suggesting the good quality of QDs. Tauc plot [Pankove, 1975] is shown in the inset of Figure 5.3b and the estimated indirect band gap of MoS_2 QDs is 1.66 eV which is in good agreement with other studies [Saha et al., 2015; Sarkar et al., 2019; Veeramalai et al., 2019] of MoS_2 QDs. The band gap of bulk MoS_2 is 1.2 eV [Eda et al., 2011]. The estimated band gap is higher than the band gap of bulk MoS_2, which indicates band gap opening because of quantum confinement due to a reduction in size [Veeramalai et al., 2019].

The x-ray photoelectron spectra (XPS) of MoS_2 QDs corresponding to Mo 3d and S 2p states have been plotted in Figures 5.3c and 5.3d, respectively. XPS curve fitting of Mo 3d indicates the existence of Mo^{4+} state mainly, which confirms the formation of MoS_2. The peaks with a binding energy of 228.8 eV and 232.0 eV corresponding to Mo $3d_{5/2}$ and Mo $3d_{3/2}$ states of

2H-MoS_2, respectively, agree well with previous data [Fan et al., 2018]. Small peaks corresponding to Mo^{6+} and Mo^{5+} states indicate the formation of a small amount of intermediated products when $(NH_4)_2MoS_4$ was reduced at high temperatures. The peak at 226.1 eV corresponds to the S 2s state. XPS curve for the S 2p state can be fitted with two curves, as shown in Figure 5.3d and the peaks with binding energy 161.8 eV and 163.3 eV correspond to $2p_{3/2}$ and $2p_{1/2}$ states of 2H-MoS_2, respectively [Fan et al., 2018].

The morphology of the QDs was shown in the AFM image with a line profile, as shown in Figure 5.3e. From the line profile, it is clear that QDs are few layers and calculated RMS roughness is around 1 nm as measured from the surface analysis.

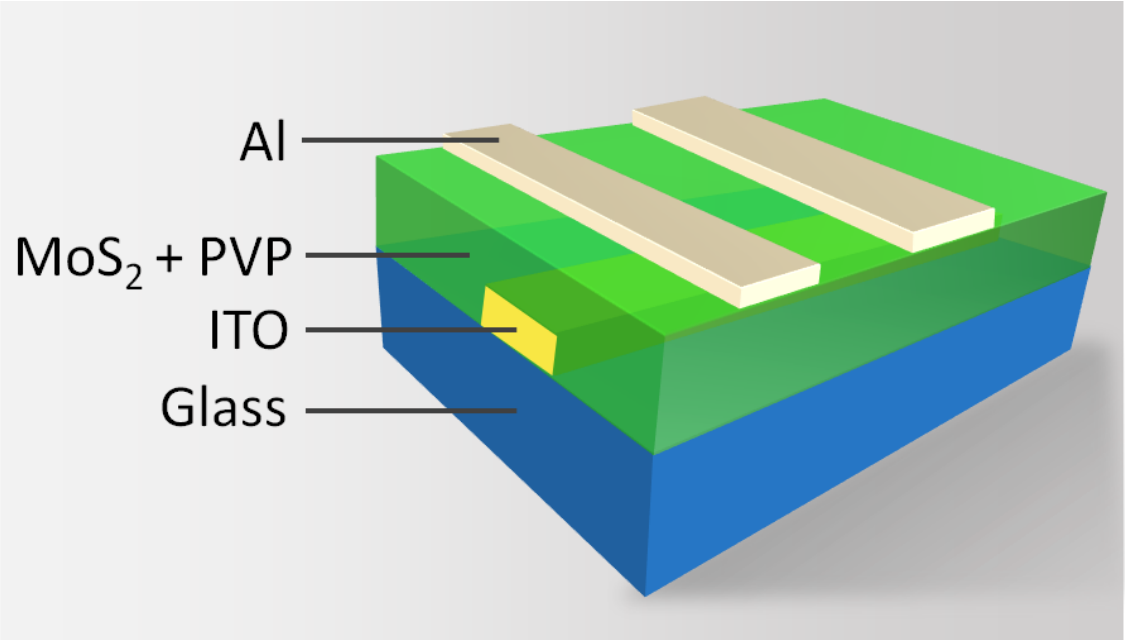


Figure 5.2: Schematic representation of the device structure.

To determine the particle size, TEM measurements were carried out by drop-casting a dilute solution of MoS_2 QDs in chloroform on a copper TEM grid. The TEM images of MoS_2 QDs are shown in Figures 5.4a and 5.4b. The TEM images indicate the spherical shape of QDs and no aggregation of particles. The statistical distribution of the size of the QDs has been plotted in Figure 5.4c. The fitted curve with the Gaussian function indicates a Gaussian distribution of the particle sizes. The estimated particle sizes vary from 3.5 nm to 6.0 nm and the mean diameter of the QDs is 4.43 nm as calculated from the distribution curve. The HRTEM image of a single QD revealed the highly crystalline nature of the QDs, as shown in Figure 5.4d. Clear lattice fringes have been observed in Figure 5.4d. From the clearly visible lattice fringes, the measured lattice spacing of 0.256 nm and 0.228 nm correspond to (100) and (110) planes of MoS_2 crystal [Veeramalai et al., 2019], respectively, which has been confirmed from the SAED pattern of MoS_2 QDs as shown in Figure 5.4e. The HRTEM images indicate the formation of high-quality MoS_2 QDs.

To determine the thickness of different layers in the fabricated device, the device was cut in the middle and the cross-sectional of the device was viewed in FESEM. Four distinct layers of glass, ITO, MoS_2-PVP and Al, have been clearly observed in the cross-sectional FESEM image of the fabricated device, as shown in Figure 5.4f. The cross-sectional FESEM image confirms that the thickness of the MoS_2 QDs-PVP active layer is around 214 nm, whereas the thickness of the top Al and bottom ITO electrodes is around 162 nm and 175 nm, respectively.

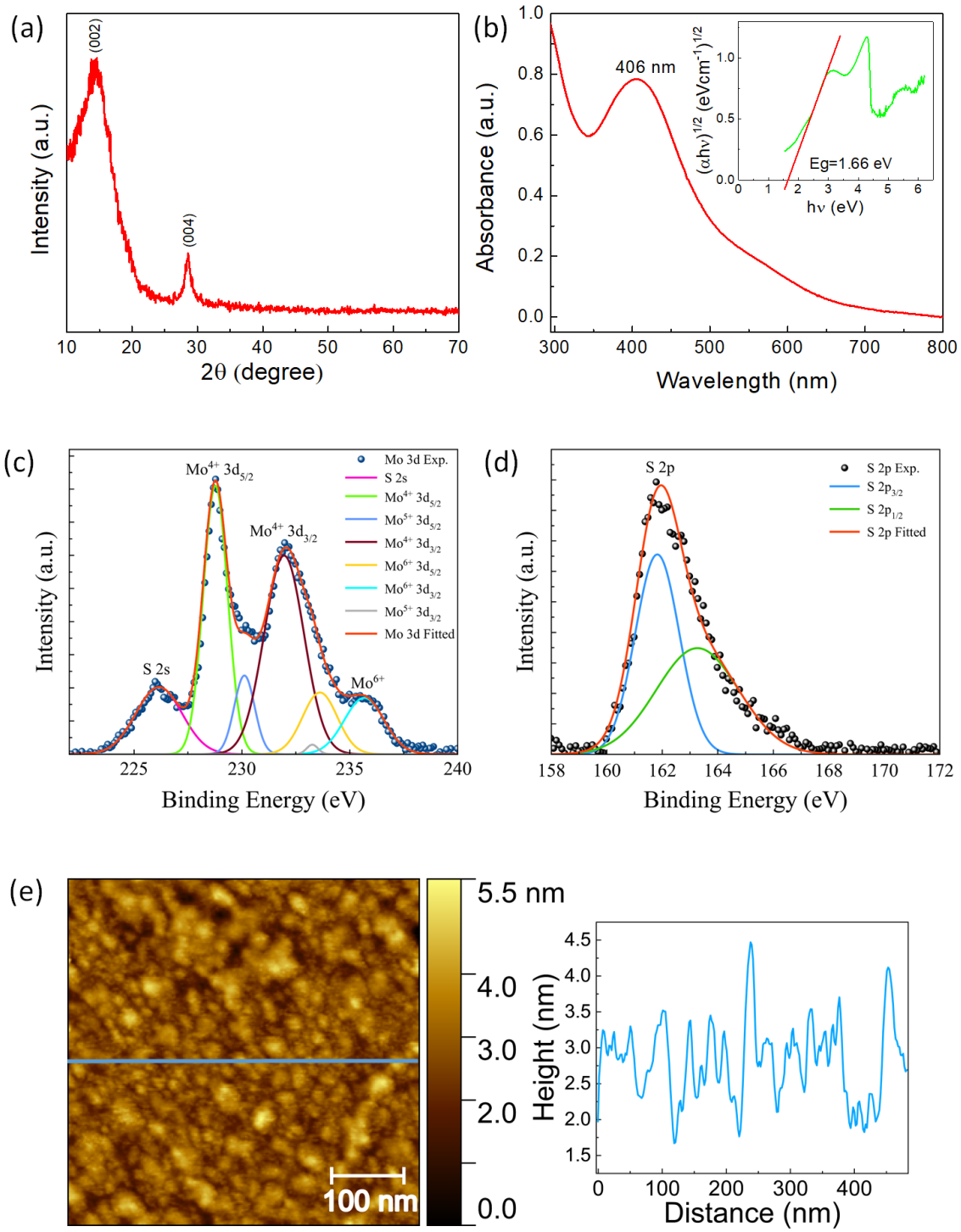


Figure 5.3: (a) XRD pattern of MoS_2 QDs. XPS spectra with curve fitting of (b) Absorption spectra of MoS_2 QDs and the inset shows Tauc plot to determine the band gap. (c) Mo 3d and (d) S 2p states of as-synthesized MoS_2 QDs. (e) AFM image of MoS_2 QDs with line profile.

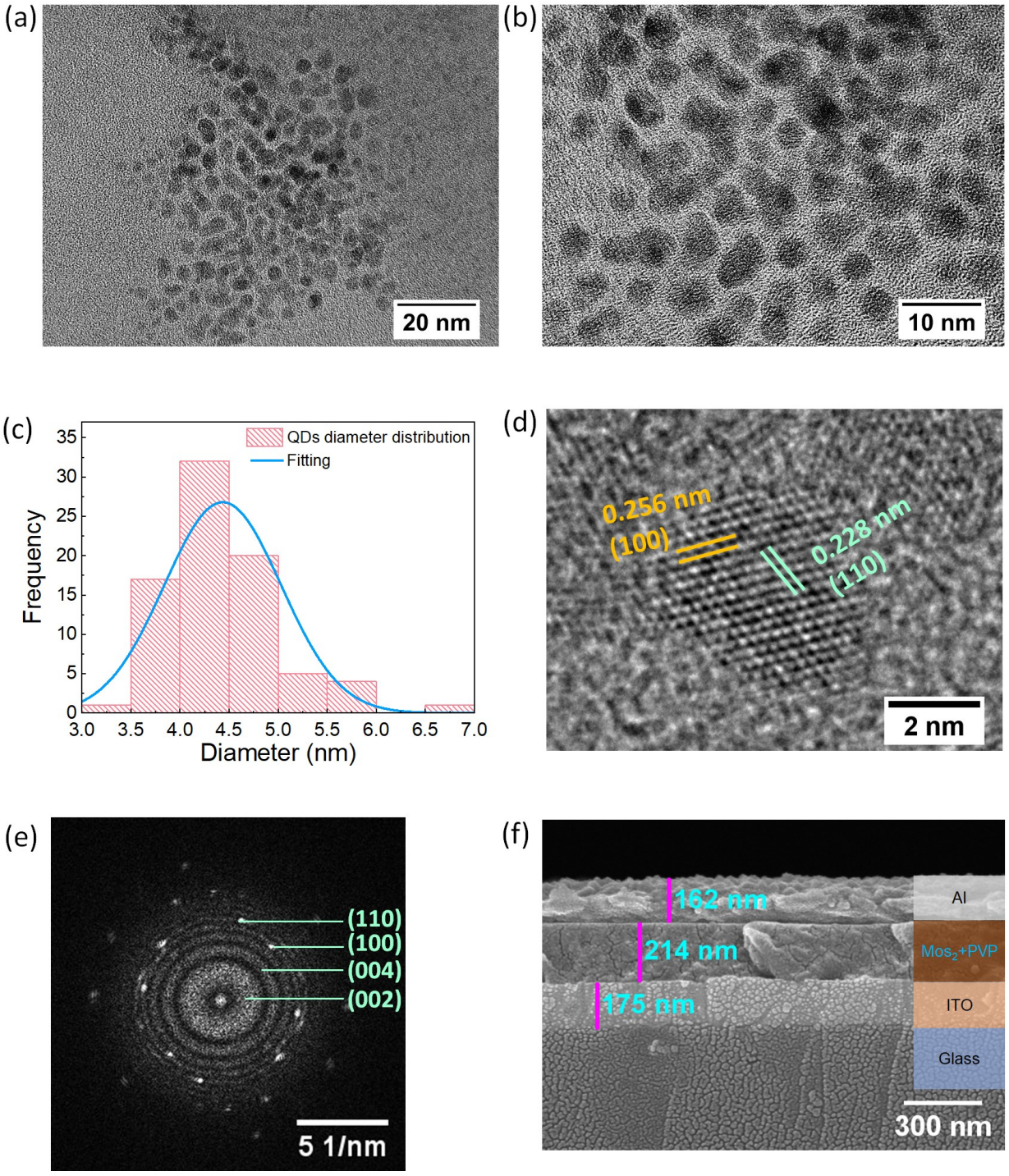


Figure 5.4: TEM image of MoS_2 QDs (a) with 20 nm scale bar (b) magnified image with 10 nm scale bar (c) statistical size distribution curve with Gaussian fitting as measured from TEM image. Mean diameter of 4.43 nm has been obtained from the size distribution curve (d) HRTEM image of a single QD with clearly visible lattice fringes. The lattice spacing of 0.256 nm and 0.228 nm correspond to (100) and (110) planes which were confirmed from the (e) SAED pattern. (f) FESEM image of a cross-sectional view of the fabricated device. The Top Al layer, an active layer of MoS_2-PVP and the bottom ITO layer is clearly visible from the FESEM image.

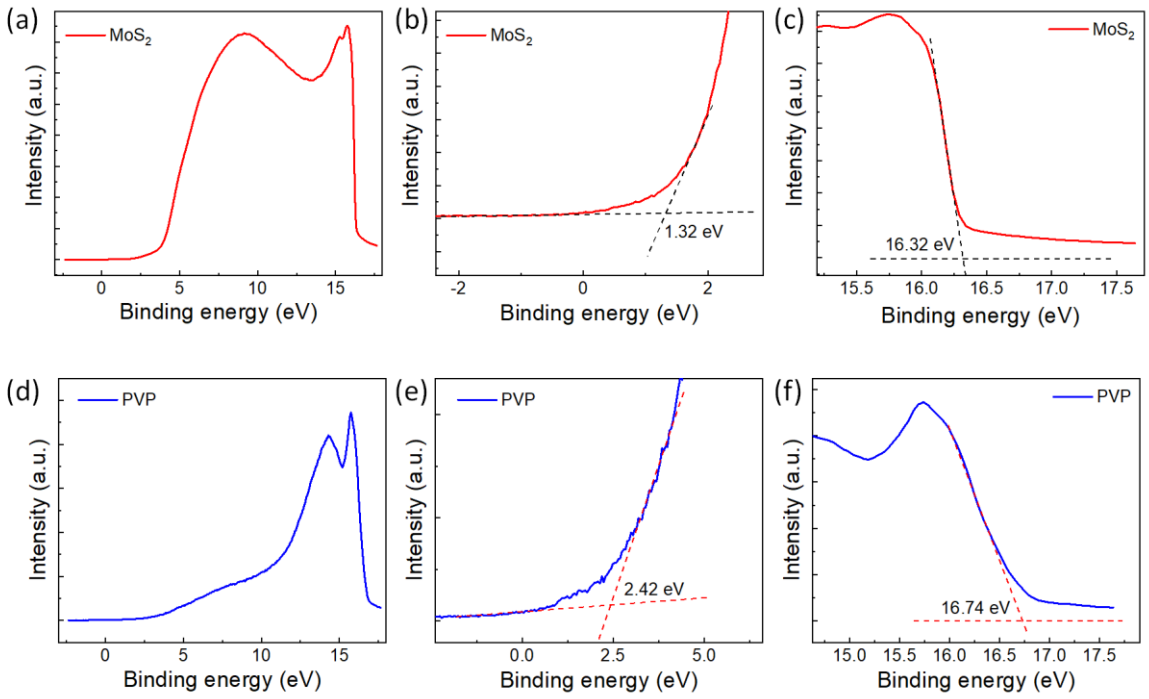


Figure 5.5: (a) Full energy range UPS spectra and magnified (b) low energy onset region (c) high energy secondary cut-off region in UPS spectra of MoS_2 QDs. (d) Full energy range UPS spectra and magnified (e) low energy onset region (f) high energy secondary cut-off region in UPS spectra of PVP.

To determine the band energy position in MoS_2 QDs and PVP, the UPS measurements were carried out in a Thermo Scientific K-Alpha+ spectrometer within ultrahigh-vacuum conditions (10^{-9} mbar) using He Iα radiation of energy 21.22 eV. The full-range UPS spectra of the MoS_2 QDs have been shown in Figure 5.5a. The magnified low energy onset region and high energy secondary cut-off region of UPS spectra of MoS_2 QDs have been shown in Figure 5.5b-c. Figure 5.5d shows the full range UPS spectra of PVP. The magnified low energy onset region and high energy secondary cut-off region of UPS spectra of PVP have been shown in Figure 5.5e-f. From the low energy onset region and high energy region, secondary cut-off values for the HOMO energy and the LUMO energy have been determined as -6.22 eV and -4.56 eV, respectively, for MoS_2 QDs. The HOMO and LUMO energy for PVP has been determined as -6.90 eV and -3.07 eV, respectively.

5.3.2 Electrical Characterizations of the Device

The I-V characteristic of the device at RT in a voltage window −1.5 V to +1.5 V is shown in Figure 5.6a. Voltages were applied to the device in a sweep pattern 0 V→ +1.5 V → 0 V → −1.5 V → 0 V. From 0 V to 1.4 V, the device is in a HRS or off state where the current is very low. As voltage increases slightly, the current jumps from 4.38×10^{-8} A to 1.26×10^{-5} A at 1.45 V, which is called the SET process and the state is LRS or on state. The device remained in LRS when the voltage was reduced from 1.5 V to 0 V and even negative voltages were applied; it still remains in LRS. When a high negative voltage is applied, the current suddenly drops from -1.5×10^{-5} A to -5.7×10^{-8}A at −1.35 V and the device switches from LRS to HRS, which is the RESET process. The ratio of current in LRS and HRS state (I_{ON}/I_{OFF}) with applied voltage has been plotted in the inset of Figure 5.6a. The highest value of I_{ON}/I_{OFF} in our device has been found to be 10^5 at −0.64 V, which is sufficiently high for a resistive memory device. The inset of Figure 5.6a shows that the current in the negative side first decreases and then increases between -0.4 V and -1 V after the RESET process. This is obtained due to the slight hysteresis in the device due to the capacitive effect caused due to the charge accumulation at the interface between the electrode and the active material [Ranjan et al., 2020; Yan et al., 2016].

To test the endurance of the device, successive sweeps over 250 cycles were applied to the device. The absolute values of current in the off and on state are recorded at −0.6 V and plotted on a logarithmic scale as a function of a number of cycles, as shown in Figure 5.6b. A significant difference between the current in HRS (off) and LRS (on) state after running 250 cycles indicates the high endurance of the device.

The retention characteristic was measured by applying an erase pulse of −1.6 V with a pulse width of 6 s and a read pulse of −0.6 V over 27000 s to record HRS current, whereas a write pulse of +1.6 V of pulse width 6 s followed by read pulse of −0.6 V over 27000 s were applied to record LRS current. The device retains the LRS and HRS states for more than 27000 s with large $I_{ON}/I_{OFF,}$ as shown in Figure 5.6c. No overlay between current in LRS and HRS state in the retention characteristic suggests that the device can be used for a long time without any degradation.

The random-access memory (RAM) characteristic was obtained by applying a train of pulses in a pattern of +1.6 V of pulse width 6 s (write) → −0.6 V of pulse width 6 s (read) → −1.6 V of pulse width 6 s (erase) → −0.6 V of pulse width 6 s (read) and recoding the current in each pulse as shown in Figure 5.6d. A clear significant difference between the read current after erase and the read current after a write was observed. This indicates that the device can be efficiently used as RAM.

The highest value of the current in the on state is around 12.43 μA at 1.5 V, while the highest value of the off current is 43 nA at 1.44 V. Therefore, the ultimate power consumption of the device is around 19 μW in the on state and 63 nW in the off state, which indicates very low power consumption for energy saving. The high value of I_{ON}/I_{OFF}, high endurance, long retention time and low power consumption in the fabricated device indicate that the less toxic and non-carcinogen material MoS_2 QDs could be a promising candidate for high-performance and low-powered resistive memory devices.

For the smooth operation of the resistive memory device in extremely high temperatures, the thermal stability of the device must be checked. In order to check the thermal stability of the device, temperature dependent I-V measurements were performed by simultaneously heating the device at a particular temperature during measurements. The device was heated by a sample stage heater attached to a homemade probe station. At first, the temperature was set to 40 °C and the temperature was stable after 10 min. When the temperature was stable at 40 °C, the I-V measurement was taken. The same procedure was applied to other temperatures also. Figure 5.7a-b shows the I-V characteristics of the device at different temperatures. The device shows resistive switching with sharp SET and RESET up to 130 °C, which suggests our device will be fully operational at very high temperatures also.

The operational speed of the device was tested by time response performance which was performed by giving an input square wave signal and recording the output signal. As shown in Figure 5.7c, the output signal from the device has a delay of 28 ns which is the response time of the device. The response time is very short in our device, suggesting the high speed of the device.

To confirm the effect of MoS_2 QDs in the PVP matrix in RS, another device with pure PVP as an active layer was prepared. The I-V characteristics of a pure PVP-based device (Al\PVP\ITO) have been shown in Figure 5.7d. From the I-V characteristics of the Al\PVP\ITO device, it is clear that the pure PVP-based device does not show significant resistive switching. The resistive switching is observed when MoS_2 QDs are embedded in the PVP matrix.

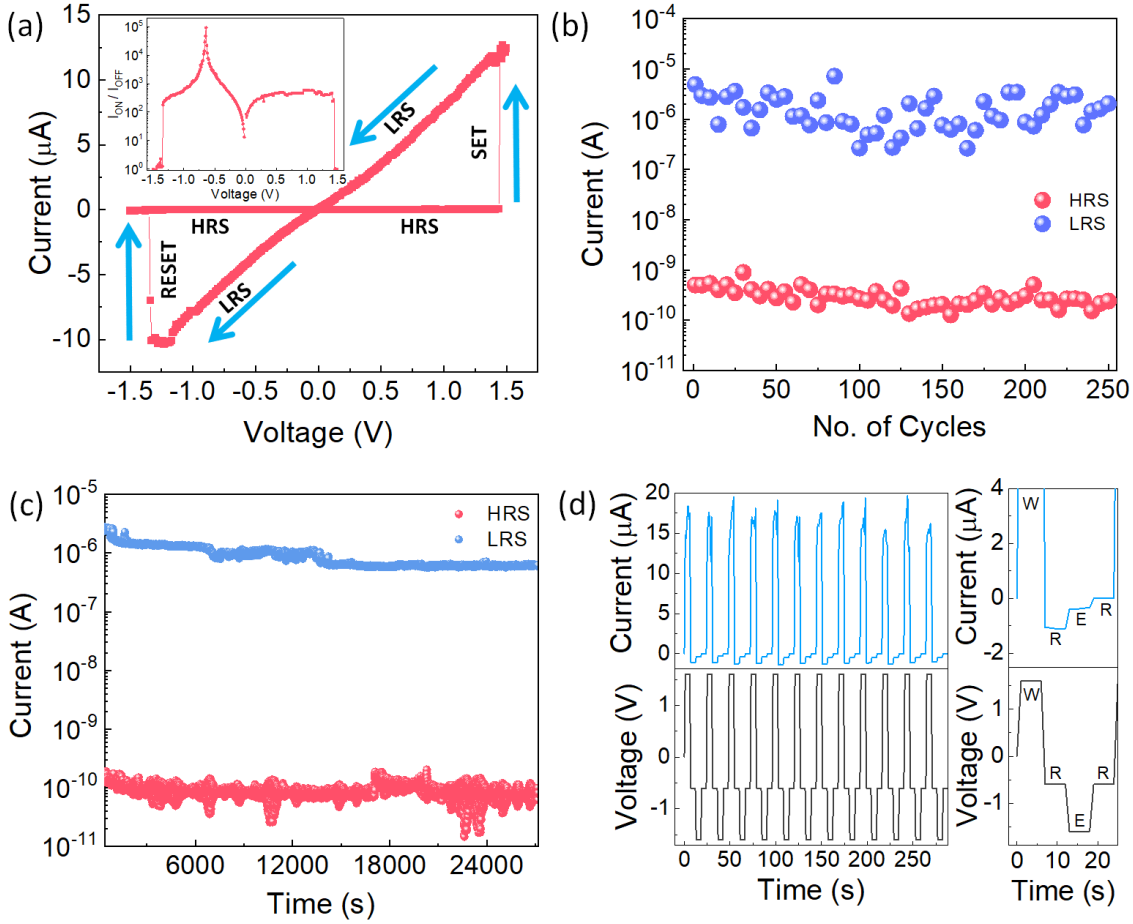


Figure 5.6: (a) I-V characteristic curve of the MoS_2 QDs-PVP device. The inset shows the variation of I_{ON}/I_{OFF} with applied bias. (b) Endurance plot at a read voltage of −0.6 V (c) Retention characteristic of the device at a read voltage of −0.6 V (d) "write-read-erase-read" sequence of the device where the enlarged view of a single complete operation is shown on right hand side.

To comprehend the charge transport mechanism, we have plotted the I-V characteristic of the device with both axes on a log scale, as shown in Figure 5.8a. In the off (HRS) state, the curve has four distinct regions. From 0 V to 0.17 V, the log(I) vs log(V) curve has a slope of 0.24, which indicates that a very less number of electrons can overcome the energy barrier between ITO and PVP. From 0.18 V to 0.53 V, the log(I) vs $V^{1/2}$ plot has a slope of 0.93 ~ 1, as shown in Figure 5.8b and in this region, $\log(I) \propto V^{1/2}$, which indicates thermionic emission behavior. In this region, thermally generated charge carriers overcome the energy barrier between ITO and PVP and take part in charge transport. The thermionic emission [Wu et al., 2019] of charge carriers can be expressed by the equation

$$I \propto T^2 \exp\left(\frac{-q\left(\emptyset_B - \sqrt{\frac{qV}{4\pi\varepsilon}}\right)}{K_B T}\right) \tag{5.1}$$

where $\emptyset_B$, ε, K_B and T are the effective Schottky barrier height, dielectric constant, Boltzmann constant and temperature. As the number of thermally generated carriers is not large, the current is low in this region. From 0.54 V to 1.13 V, the current-voltage has a linear relationship which indicates the generation of free charge carriers due to thermal energy (Betal et al., 2022; Bhattacharjee et al., 2017; Shin et al., 2016; Thomas et al., 2020; Wang et al. 2020b; Yang et al. 2017). From 0.55 V to 1.44 V, log(I) vs log(V) curve can be fitted with a slope of 2 which means $I \propto V^2$ at this region. In this stage, the charge transport mechanism is due to the SCLC [Joung et al., 2010] (space charge limited current) process, which can be expressed as

$$I \propto \frac{\mu\varepsilon n}{n_t}(V^2/d^3) \tag{5.2}$$

where μ, n, n_t and d are the mobility of the charge carrier, the effective density of states, the concentration of the trapped charge and the thickness of the sample, respectively. After the SCLC process, further increment in voltage causes the SET process of the device. In the ON state, the current is high and the log(I) vs log(V) curve can be fitted with a slope of 1, which indicates ohmic conduction takes place.

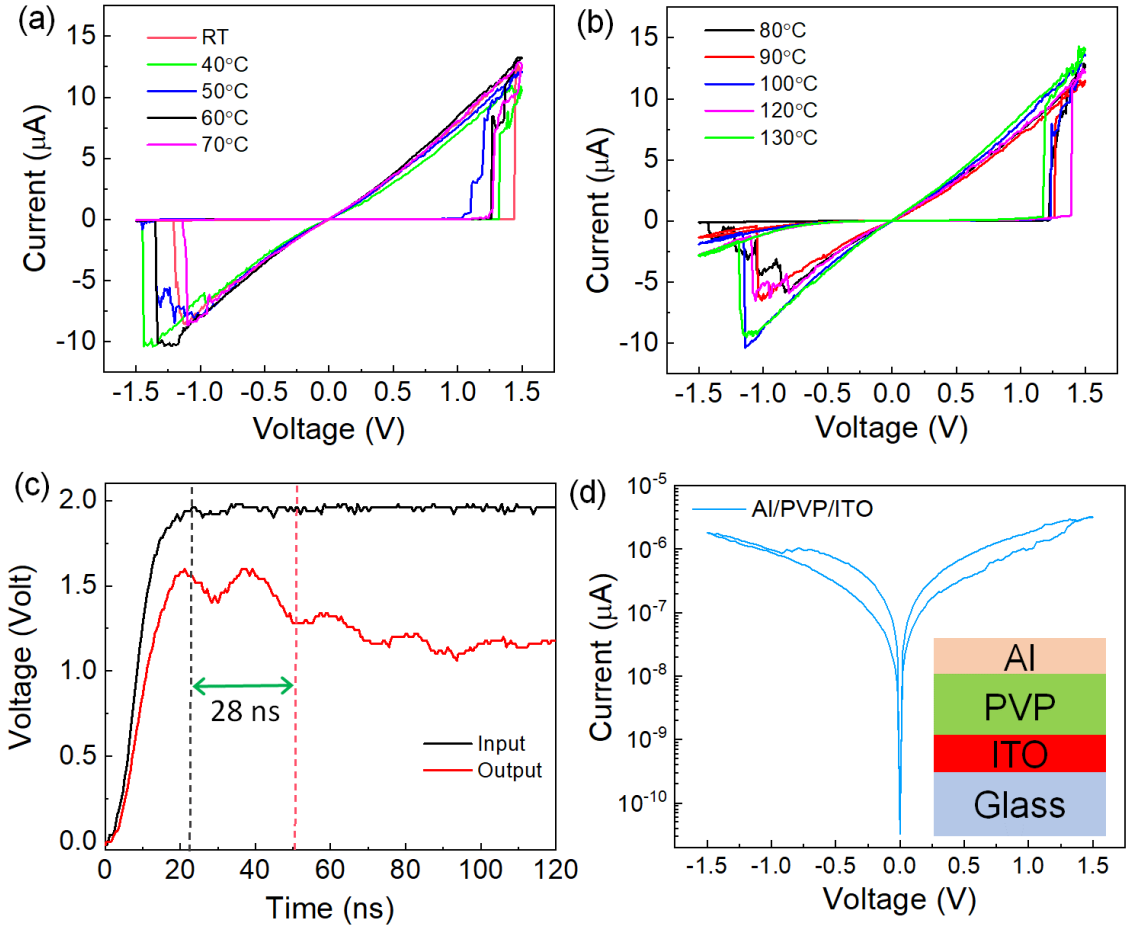


Figure 5.7: I-V characteristic curve of the MoS_2 QDs-PVP device at (a) RT, 40 °C, 50 °C, 60 °C, and 70 °C, (b) 80 °C, 90 °C, 100 °C, 120 °C and 130 °C. (c) Response time of the device by applying a square wave pulse of 2 V (V_{pp}) with a pulse width of 50 μs. (d) The I-V characteristic of pure PVP-based (Al\PVP\ITO) device. The pure PVP-based device does not exhibit significant resistive switching.

To give more insight into the conduction mechanism, energy band diagrams have been plotted in Figure 5.9. Figure 5.9a shows the energy band diagram of the device at zero bias. The energy band positions of MoS_2 QDs and PVP have been determined using ultraviolet photoelectron spectroscopy (UPS), as shown in Figure 5.5. When a small positive voltage is applied to the Al electrode, energy bands are bent, as shown in Figure 5.9b and a small number of injected electrons from ITO can overcome the energy barrier between PVP and ITO. An increment in voltage results reduction of the energy barrier between PVP and ITO and thermally generated electrons will be injected from ITO to PVP. After entering into PVP, these injected electrons will be trapped in the defect sites present in the MoS_2 QDs. The defect sites in MoS_2 QDs act as trapping and de-trapping centers for electrons. Very few electrons can reach from the bottom electrode to the top electrode, which results in low current in the off state. The conduction mechanism takes place because of thermally generated free electrons until trapped electrons density overcomes the free electrons density. As voltage increases, more injected electrons will be trapped in the trapping centers. Further increment in voltages led to rapid filling of most of the trap sites and the conduction mechanism is due to the SCLC process at this stage. As most of the trapping centers are already filled by the electrons, further increment in voltage induces a conductive channel through the insulating PVP matrix, which results in an abrupt increment in

the current and SET process occurs. At this stage, the injected electrons can easily reach the top electrode, as shown in Figure 5.9c. An ohmic conduction takes place in the on state because of the formation of a conductive path. The device remains in the on state even in negative voltage until the destruction of the conductive channel occurs. At high negative voltage, the electrons are de-trapped from the trapping centers, which results in the breaking of the conductive channel. As the conductive channel breaks at this stage, the device goes to the off state and the RESET process occurs. In the off state, only those electrons which were in trapping centers will be de-trapped and take part in the conduction mechanism, as shown in Figure 5.9d. As a pure PVP-based device does not show significant resistive switching (Figure 5.7d), the incorporation of MoS_2 QDs in the PVP matrix plays a significant role in switching behavior in MoS_2 QDs-PVP based device.

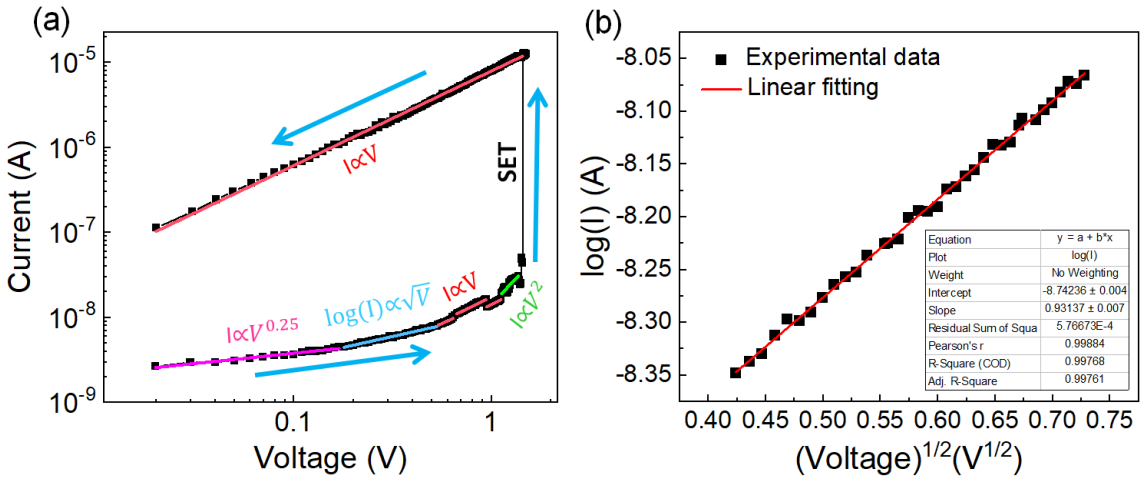


Figure 5.8: (a) The log(I) vs log(V) plot of the device for the positive sweep. (b) The log(I) vs $V^{1/2}$ plot in the voltage range 0.18 V to 0.53 V in the OFF state and in this region log(I) $\propto V^{1/2}$.

5.4 Conclusions

In this chapter, a MoS_2 QDs-PVP nanocomposite-based RRAM device has been demonstrated. The colloidal MoS_2 QDs were synthesized using thermal reduction of ammonium tetrathiomolybdate ($(NH_4)_2MoS_4$) in a nitrogen atmosphere. The fabricated device shows excellent nonvolatile RS behavior. The device exhibits a maximum I_{ON}/I_{OFF} of 10^5 with high endurance, long retention, fast response time and excellent RAM characteristics. The ultimate power consumption by the device is considerably low. The ultimate power consumption of the device is around 19 µW in the on state and 63 nW in the off state, which indicates very low power consumption for energy saving. In addition, the resistive switching stability of the device at different temperatures has been explored. The MoS_2 QDs-PVP based RRAM device shows RS behavior even at 130 °C, which reveals that it can be operated in a hot region also. The RS behavior is mainly due to the trapping and de-trapping of electrons in the MoS_2 QDs because MoS_2 QDs act as charge trapping centers and the PVP act as a charge blocking layer. The high I_{ON}/I_{OFF}, high endurance, long retention time, low power consumption, fast response time and excellent temperature stability in the fabricated device indicate that the less toxic and non-carcinogen material MoS_2 QDs could be a promising candidate for high-performance and low-powered resistive memory devices which can be operated in hot environment conditions also.

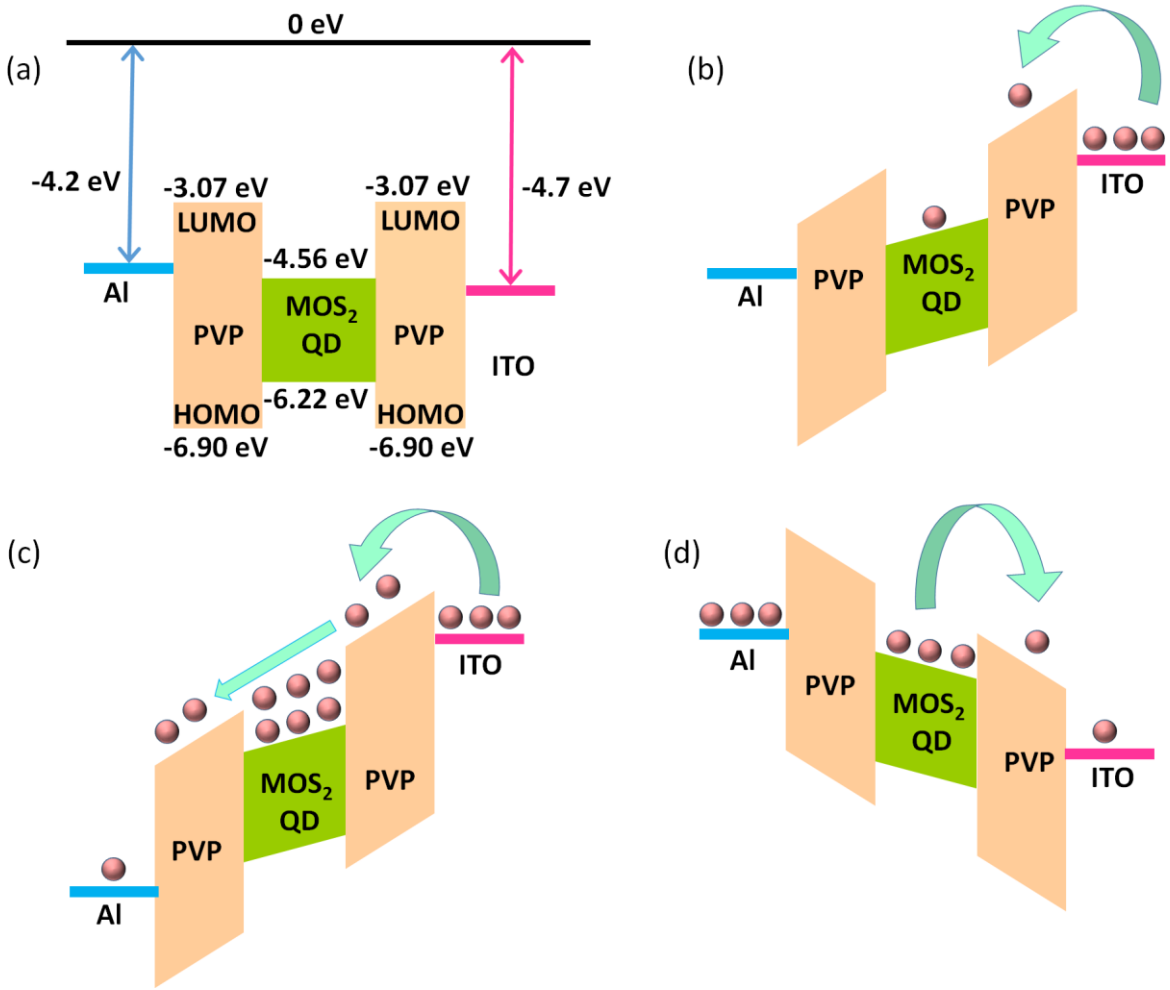


Figure 5.9: The energy band diagram of the device at (a) zero bias (b) small positive bias where electrons are getting trapped by the MoS_2 QDs (c) high positive voltage and SET process, where a conductive channel through the PVP matrix is established as most of the vacant cites, were already filled by injected electrons (d) negative bias where breaking of the conductive channel occurs and conduction is due to the release of the trapped charges from the trapping centers.